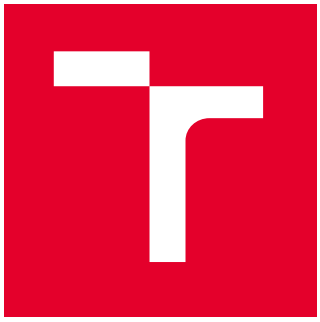

BRNO UNIVERSITY OF TECHNOLOGY

VYSOKÉ UČENÍ TECHNICKÉ V BRNĚ

FACULTY OF MECHANICAL ENGINEERING

FAKULTA STROJNÍHO INŽENÝRSTVÍ

INSTITUTE OF PHYSICAL ENGINEERING

ÚSTAV FYZIKÁLNÍHO INŽENÝRSTVÍ

OPTICAL DICHROISM IN VORTEX ELECTRON ENERGY-LOSS SPECTROSCOPY

OPTICKÝ DICHROISMUS VE SPEKTROSKOPII ENERGIOVÝCH ZTRÁT VORTEXOVÝCH ELEKTRONŮ

BACHELOR'S THESIS

BAKALÁŘSKÁ PRÁCE

AUTHOR

AUTOR PRÁCE

Martin Ošmera

SUPERVISOR

VEDOUCÍ PRÁCE

Ing. Andrea Konečná, Ph.D.

BRNO 2022

BRNO UNIVERSITY OF TECHNOLOGY
FACULTY OF MECHANICAL ENGINEERING

Assignment Bachelor's Thesis

Institut:	Institute of Physical Engineering
Student:	**Martin Ošmera**
Degree programm:	Physical Engineering and Nanotechnology
Branch:	no specialisation
Supervisor:	**Ing. Andrea Konečná, Ph.D.**
Academic year:	2021/22

As provided for by the Act No. 111/98 Coll. on higher education institutions and the BUT Study and Examination Regulations, the director of the Institute hereby assigns the following topic of Bachelor's Thesis:

Optical dichroism in vortex electron energy–loss spectroscopy

Brief Description:

Transmission electron microscopy is one of the fundamental techniques suitable not only for imaging samples with atomic resolution but it can also be used together with spectroscopic techniques, such as electron energy–loss spectroscopy, which is capable of detecting energy transfer between the electron beam and probed sample. One of the new possibilities is to employ vortex electron beams, which in the interaction with samples exchange energy and also orbital angular momentum that is manifested in dichroism in electron energy–loss spectra. The use of electron vortices is especially suitable for probing chiral or magnetic samples whose response would be otherwise undetectable.

In this thesis, the interaction of vortex electrons with chiral nanostructures (e.g. plasmonic antennas of special shapes) will be explored. Both numerical and analytical descriptions will be used in limiting cases. One of the possible goals will be to find experimental conditions and parameters (e. g. focusing of the beam, magnitude of the orbital angular momentum, initial beam energy) for maximization of the detected dichroic signal.

Bachelor's Thesis goals:

1) Review of electron energy–loss spectroscopy (EELS) and vortex electron beams (VEBs). Study the possibilities of theoretical description of inelastic interaction of VEBs with different types of samples.
2) Model analytically EELS for VEBs interacting with point chiral objects. Try to find computationally suitable experimental parameters for the maximisation of dichroic EELS signal.
3) Get to know existing programmes for the numerical solution of Maxwell's equations (e.g., Comsol Multiphysics, MNPBEM toolbox for Matlab) and try to implement the interaction of VEBs with chiral nanostructures within these programmes.

Recommended bibliography:

GARCÍA DE ABAJO, F. J. Optical excitations in electron microscopy. Rev. Mod. Phys., 82 (2010), 209-275.

ASENJO-GARCÍA A., and GARCÍA DE ABAJO, F. J. Dichroism in the interaction between vortex electron beams, plasmons, and molecules. Phys. Rev. Lett., 113 (2014), 066102.

ZANFROGNINI, M., et al. Orbital angular momentum and energy loss characterization of plasmonic excitations in metallic nanostructures in TEM. ACS Photonics, 6 (2019), 620-627.

Deadline for submission Bachelor's Thesis is given by the Schedule of the Academic year 2021/22

In Brno,

L. S.

prof. RNDr. Tomáš Šikola, CSc. Director of the Institute	doc. Ing. Jaroslav Katolický, Ph.D. FME dean

Objectives which should be achieved

1. Review of electron energy-loss spectroscopy (EELS) and vortex electron beams (VEBs). **Study the possibilities of theoretical description of inelastic interaction of VEBs with different types of samples.**

2. Model analytically **EELS for VEBs interacting with point chiral objects**. Try to find computationally suitable experimental parameters for the **maximisation of dichroic EELS signal.**

3. Get to know existing programmes for the numerical solution of Maxwell's equations (e.g., Comsol Multiphysics, MNPBEM toolbox for Matlab) and try to implement the interaction of VEBs with chiral nanostructures within these programmes.

Raw Outline of the Thesis

Introduction

1. Chirality and dichroism
    - What does chrality mean?
        - Picture of hands (etymology of the term)
        - Properties of chiral structures?
        - Chirality of molecules – examples!
        - Properties of chiral molecules
          + Optical Activity (mechanism? and use in spectroscopy)
          + Chirality and enantiomers – Drugs and Healthcare (Thalidomid)
        - Chirality of VEBs and their properties
    - Measurement and Dichroism
        - dichroism (literally, "two-colored")
        - dichroism in nature (bug shells etc.)

2. Electron energy loss spectroscopy (EELS) with Vortex Electron Beams (VEBs)
    - Principles of method
    - EEL spectrum function
    - Vortex electron Beams (VEBs)
        - Theory of VEB formation +Laugere–Gaussian beams
        - Methods of preparation
        - Properties of VEBs (in comparison with standard electron beams)
        - Analytical model

3. Semi–Analytical model of VEB's interaction with a chiral point object
    - Maximization of dichroic EEL spectrum

4. Numerical analysis

- Boundary Element Method (BEM)
  - derivation from Maxwells equations
- Numerical model of VEB's interaction with a nanohelix using MNPBEM toolbox for Matlab

Abstract

Lorem ipsum dolor sit amet, consectetur adipisici elit, sed eiusmod tempor incidunt ut labore et dolore magna aliqua. Ut enim ad minim veniam, quis nostrud exercitation ullamco laboris nisi ut aliquid ex ea commodi consequat. Quis aute iure reprehenderit in voluptate velit esse cillum dolore eu fugiat nulla pariatur. Excepteur sint obcaecat cupiditat non proident, sunt in culpa qui officia deserunt mollit anim id est laborum. »>XXX«<

Key Words

EELS, Vortex electron beams, optical dichroism

Abstrakt

Měsíční kamení říká, že bědovat nad šedivostí ďábelských démonů češství, ťukaje si na čelo, dým nepřináší a život ani úpění skřehotajících žab na slať nevrátí, člověka nevyžene a kočka bude mňoukat dál.

Klíčová slova

OŠMERA, Martin. *Optical dichroism in vortex electron energy–loss spectroscopy.* Brno, 2022. URL: https://www.vutbr.cz/studenti/zav-prace/detail/139390. Bachelor's thesis. Brno University of Technology, Faculty of Mechanical Engineering, Institute of Physical Engineering. Supervisor Andrea Konečná.

Acknowledgement

Hereby I thank...

Contents

Introduction

Chapter 1

Electron Energy Loss Spectroscopy with Vortex Electron Beams

Through the last century, the need of mankind to look at small things grew rapidly. One of the approaches used to gain better spatial resolution is to enslave electrons instead of photons. Electrons are particles with a non-zero rest mass. Thanks to that, we can get the same spatial resolution with relatively less energy in imaging with electrons compared to light. It is also incomparably easier to manipulate (focus) charged particles as electrons compared to high-energy light such as x-rays.

The first step in electron microscopy is the generation of electrons. This is done by pulling the electrons from a cathode by electric field. The cathode can be heated to lower the difference between thermal energy of the electrons in the specimen and work function of the cathode. In state-of-the-art designs of electron microscope, however cold (room temperature) cathode is used, mainly because the gained electron beam has narrower energy distribution.

Electrons pulled from the cathode are then collimated and shaped into a well-controlled beam. Electron optics consisting of electrostatic and magnetic lenses is used to focus and further manipulate the beam e. g. for scanning. The beam profile can be further modified for different uses. Nowadays, beam currents can be so low that less than one electron is present in the microscope column at one moment. The beam profile can be then understood as the square modulus of the electron's wave function. As we will demonstrate in Secs. 1.1.1 and 1.1.2 electron beams can be tailored not only in amplitude but in the phase domain too.

There are generally two types of electron microscope designs, scanning and transmission. In a Scanning Electron Microscope (SEM) the electron beam is scanned over the specimen and different types of emitted particles (e.g. secondary electrons, Auger electrons, backscattered electrons, cathodoluminiscence, x-ray etc.) are detected, revealing different pieces of information about the point on specimen in which the beam is currently directed. The image is then constructed by attributing the measured signal to each point of the rastered mesh. The specimen can be thick (it has to fit into the microscope chamber) but must be conductive. Non-conductive specimens are thus cover in thin metallic layer.

The second class of electron microscopes are Transmission Electron Microscopes (TEMs) which work similarly as traditional optical microscopes in which the light transmits through the specimen. Transmitted electrons construct a "true" image on a screen or a CCD chip. Should electrons pass through the specimen, we typically need much higher accelerating voltage and very thin specimens ($\lesssim 100\,\mathrm{nm}$, this is probably the main disadvantage of TEM). Electrons in a typical TEM have energies around $30\,\mathrm{keV}$ (with speed $0.33\,c$) but can reach up to $300\,\mathrm{keV}$ ($0.77\,c$). Such electron beam can be focused to spot with diameter $\lesssim 0.1\,\mathrm{nm}$

[1, 13], this leads to a very good lateral resolution since interatomic distances are typically in orders of 10^{-1}nm.

There exists an interesting combination of both previous approaches: Scanning Transmission Electron Microscopy (STEM). In STEM, high energy electron beam is scanned over a thin specimen. Severeal signals can be measured: transmited electrons, high angle diffracted electrons, cathodoluminiscence etc. Beside the topographic view, STEM can be operated in tomographic mode getting us full spatial information about specimens.

We need not only to see the topography of the specimens but also to characterize their material and excitations residing in them (in the best scenario together with the spatial layout). For this purpose STEM offers several spectroscopic methods (e.g. cathodoluminiscence (CL) or energy dispersive x-ray (EDX)). One of them is Electron Energy-Loss Spectroscopy (EELS) which is preferentially used in Scanning Transmission Electron Microscopy (STEM). This method enables us to characterize the specimen by electron energy loss spectral function (spectrum) (EELSF) which will be discussed later in Sec. 1.3.

1.1 Vortex Electron Beams (VEBs)

Before we present electron vortices (vortex electron beams, VEs), we should mention their predecessors in light. When circularly polarized, photons carry spin angular momentum $\pm\hbar$ where the sign depends on the direction of spin of the polarization vector. This was shown in 1935 by Beth [4]. Linearly polarized photons can carry angular momentum in the direction of propagation too. It is called orbital angular momentum (OAM) and is quantized by topological charge l, so that the total OAM size is $l\hbar$. The wavefront of photon carrying OAM can be written as

$$\psi_{\mathrm{LG}}(r,\phi) \propto \mathrm{e}^{\mathrm{i}\,l\,\phi}\, L(r), \tag{1.1}$$

Where $L(r)$ is Laguerre function dependent on radial coordinate r and ϕ is the angle coordinate in cylindrical coordinate system. [19]

This led physicists to the idea of similar manner in electron optics. It is known that electrons have spin angular momentum $\pm\hbar/2$. OAM is trivially carried by bound electrons in atoms or molecules. In free electrons, it was a new thing in 2010. First to produce VEs were Uchida and Tonomura in 2010 [16]. About the methods of preparation we further write in Sec. 1.1.2.

Electrons carrying OAM differ from photons in several aspects. They have charge, mass and always have spin momentum. They thus react to electromagnetic field and they can be used to probe circular magnetic dichroism [19]. There is also (as we will explain more deeply later) possibility to use VEs to study chiral materials and structures. Verbeeck [20] also showed that VEs can be used (similarly as optical tweezers) to manipulate nanostructures in space.

In the center of the vortex, there is a phase singularity. This singularity makes the vortex beam chiral, which means that the vortex is not same as its mirror image, i.e. $psi_{+l} \neq psi_{-l}$. Phase singularities can be observed in nature as well as chirality, which has enormous importance in biology and chemistry. There exists a lot of molecules such as DNA (deoxyribonucleic acid), proteins, otherpolymers or simple molecules with four different groups on one carbon atom which are chiral. A lot of chiral molecules exists naturally only in one enantiomer or the enantiomers have completely different behaviours. If a chiral structure A (e.g. the VE) interacts with two enantiomorphs of chiral structre B and $\bar{B}$, the symmetry is

broken and we can expect different reponses from AB vs $A\bar{B}$ interaction. This phenomenon can be called dichroism and is studied in this thesis.

Electron vortices probably appear commonly in everyday TEM measurements (e.g. in materials with varying thickness) and Uchida suggests they could be used in contrast enhancement [16].

IF TIME WILL BE, ADD ISUALISATIONS OF VORTICES.

1.1.1 Theoretical Description of VEB Formation

In this section, we will show a relatively simple derivation of a formula for a wave function corresponding to a VEB used later within this work. We start with the stationary Schrödinger's equation

$$\hat{\mathbf{H}}\psi = E\psi, \tag{1.2}$$

where E is a constant (with the meaning of energy) and the Hamiltonian for a free electron of mass m can be written as

$$\hat{\mathbf{H}} = -\frac{\hbar^2}{2m}\nabla^2, \tag{1.3}$$

with $\hbar$ denoting the reduced Planck's constant. It can be shown, by simple substitution into the Schrödinger's Eq. (1.2), that a plane wave propagating along the z axis described as

$$\psi(x, y, z) = \psi(z) = \psi_0 \exp\left(\mathrm{i}\, q_z z\right), \tag{1.4}$$

where ψ_0 is a complex amplitude of the wave and q_z its wave vector, is a solution of the equation if and only if

$$E = \frac{\hbar^2 q_z^2}{2m}. \tag{1.5}$$

However, such wave function can not be normalized through the whole space. This should be no problem if we assume that the electron is captured in a finite volume (e.g. the electron microscope), which however has dimensions much larger than the electron wave function's wavelength. Near the center of the potential pit, such wave function will be very similar to the wave function of the free electron. Thus we can normalize the wave function only through the volume of the pit. Similar reasoning can be used in the center of a wavepacket [5].

We now examine the plane wave function impinging on a semi–permeable phase plate. We will consider this plate to be infinitesimally thin, allowing us to describe it by a simple complex function of transmission $T(x', y')$ defined for the x', y' plane perpendicular to z axis at the coordinate z', in which we have positioned the phase plate as schematically shown in Fig. 1.1. From the law of conservation of energy, such function must fulfil the condition $|T(x', y')| \leq 1$. Concrete real world realisations of such plates will be discussed in Sec. 1.1.2.

Just after the wave passes through the plate, the wave function changes to $\psi_\mathrm{t} = T\psi_\mathrm{i}$, where ψ_i is the wave function just before the phase plate. By applying the Huygens principle, every point on the wave front is by itself a source of spherical wave. In the paraxial approximation it is sufficient to consider the wave to spread evenly in all directions. This leads us to solving the diffraction integral.

To find the wave propagating beyond the plane z' to a plane $z > z'$, we can integrate all the contributions of spherical waves coming from points of plane z'. The spherical wave

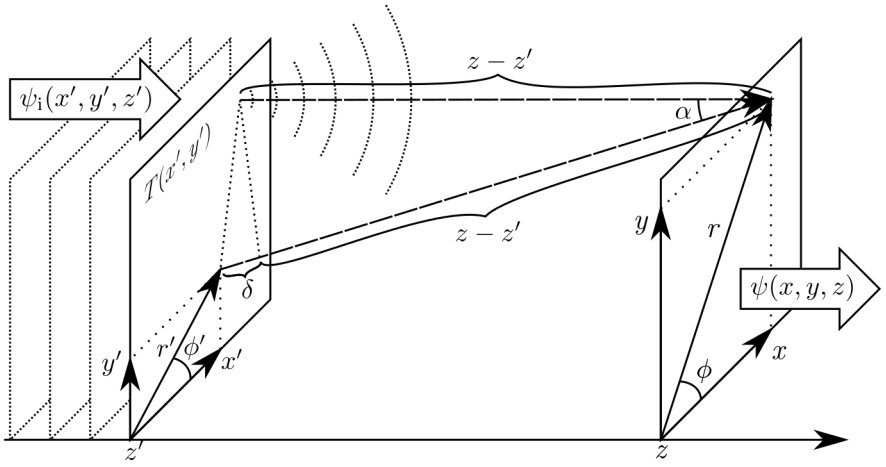

Figure 1.1: Scheme for the construction of the diffraction integral.

with wave number q coming from a point $\mathbf{r}'$ to a point $\mathbf{r}$ with an initial complex amplitude ψ_0 can be written as

$$\psi_{r'}(\mathbf{r}) = \psi_0 \frac{\mathrm{e}^{\mathrm{i}\, q|\mathbf{r}-\mathbf{r}'|}}{|\mathbf{r}-\mathbf{r}'|}, \tag{1.6}$$

where the denominator is a consequence of the law of conservation of energy. To find the total wave, we need to integrate over all the source points. In our particular case this will be the phase plate and using notation depicted in Fig. 1.1, we can find the wave in any point of the z plane as

$$\psi(x, y, z) = -\frac{\mathrm{i}\, q_z}{2\pi} \iint \mathrm{d}x'\, \mathrm{d}y'\, \psi_i(x', y', z')\, T(x', y')\, \frac{\mathrm{e}^{\mathrm{i}\, q_z (z - z' + \delta)}}{z - z' + \delta} \tag{1.7}$$

where we have assumed that electron is moving mainly along z axis so that $q_x, q_y \ll q_z \cong q$. The prefactor $-\mathrm{i}\, q_z/2\pi$ corrects the amplitude and phase of the secondary waves, as shown in [9].

Being in the paraxial space, we may use the square root approximation rule (see A.3) and from the geometry of the problem, we can find the path deviation δ (which is responsible for the interference at z plane) as

$$\delta = |\mathbf{r} - \mathbf{r}'| - (z - z') = (z - z)' \left[\sqrt{1 + \frac{(x - x')^2 + (y - y')^2}{(z - z')^2}} - 1 \right] \cong \frac{(x - x')^2 + (y - y')^2}{2(z - z')}, \tag{1.8}$$

Thanks to the paraxial aproximation, we can assume that for the denominator of the integrand in Eq. (1.7) $z - z' + \delta \cong z - z'$. With these simplifications, we can pull some terms in front of the integral and get

$$\psi(x, y, z) = -\frac{\mathrm{i}\, q_z}{2\pi} \frac{\mathrm{e}^{\mathrm{i}\, q_z (z - z')}}{z - z'} \iint \mathrm{d}x'\, \mathrm{d}y'\, \psi_i(x', y', z')\, T(x', y') \exp\left[\mathrm{i}\, q_z \frac{(x - x')^2 + (y - y')^2}{2(z - z')} \right]. \tag{1.9}$$

From now on, it will be convenient to work in cylindrical coordinates. Using the transformation rules (see A.4) we get the integral in Eq. (1.7) transformed as

$$\psi(r,\phi,z) = -\frac{\mathrm{i}\,q_z}{2\pi}\frac{\exp\left[\mathrm{i}\,q_z\left(z-z'+\dfrac{r^2}{2(z-z')}\right)\right]}{z-z'} \times \iint r'\,\mathrm{d}r'\,\mathrm{d}\phi'\,\psi_i(r',\phi',z')\,T(r',\phi')\exp\left[\frac{\mathrm{i}\,q_z}{2(z-z')}\left(r'^2-2rr'\cos(\phi-\phi')\right)\right]. \quad (1.10)$$

If we now assume that the wave incident on phase plate is a simple plane wave $\psi_\mathrm{i}(r',\phi',z') = \psi_0'\exp(\mathrm{i}\,q_z z')$ in the z' plane, we can write

$$\psi(r,\phi,z) = -\frac{\mathrm{i}\,q_z}{2\pi}\frac{\psi_0\exp(\mathrm{i}\,q_z z)}{z-z'}\exp\left(\frac{\mathrm{i}\;q_z r^2}{2(z-z')}\right) \times \iint r'\,\mathrm{d}r'\,\mathrm{d}\phi'\,T(r',\phi')\exp\left[\frac{\mathrm{i}\,q_z}{2(z-z')}\left(r'^2-2rr'\cos(\phi-\phi')\right)\right]. \quad (1.11)$$

The equation above is still rather universal. All possible transmission functions can be used to get multifarious results of outcoming waves. Also, it is possible for multiple different T's to result into similar waves. We shall now take a look at a particular example, where the transmission function takes the form

$$T(r',\phi') = \mathrm{e}^{\mathrm{i}\,l\phi'} \qquad \text{for } l\in\mathbb{Z}. \quad (1.12)$$

This transmission function characterizes a non–absorbing ($|T| = 1$ in every point) phase plate with a singularity in the middle. It might be surprising that such function is practically well-achievable, as we'll show later. Finally, our resulting wave function will be

$$\psi_l(r,\phi,z) = \frac{-\mathrm{i}\,q_z\,\psi_0}{2\pi(z-z')}\exp\left(\frac{\mathrm{i}\,q_z r^2}{2(z-z')}\right)\iint r'\,\mathrm{d}r'\,\mathrm{d}\phi'\,\mathrm{e}^{\mathrm{i}\,l\phi'}\exp\left[\frac{\mathrm{i}\,q_z}{2(z-z')}\left(r'^2-2rr'\cos(\phi-\phi')\right)\right]. \quad (1.13)$$

Analytical solution of this integral can be found in [2].

In practice, however, the beam from the diffraction plate is often focused by electromagnetic lenses to the specimen plane. Transmission through an ideal thin focusing lens is then described by another exponential function

$$F(r') = \exp\left(-\mathrm{i}\,q_z\frac{r'^2}{2f}\right), \quad (1.14)$$

where f is the focal length of the lens. If the lens plane coincides with the phase plate, its transmission function is added in the original diffraction integral:

$$\psi_l(r,\phi,z) = -\frac{\mathrm{i}\,q_z}{2\pi}\frac{\psi_0}{z-z'}\exp\left(\frac{\mathrm{i}\,q_z r^2}{2(z-z')}\right)\iint r'\,\mathrm{d}r'\,\mathrm{d}\phi'\,\mathrm{e}^{\mathrm{i}\,l\phi'}\exp\left[-\mathrm{i}\,q_z\frac{r'^2}{2f}\right]\exp\left[\mathrm{i}\,q_z\frac{r'^2}{2(z-z')}\right] \times \exp\left[\mathrm{i}\,q_z\frac{-rr'\cos(\phi-\phi')}{z-z'}\right]. \quad (1.15)$$

If $f = z - z'$, the two exponentials in the first line come off leaving us with

$$\psi_l(r,\phi,z) = -\frac{\mathrm{i}\,q_z}{2\pi}\frac{\psi_0}{z-z'}\exp\left(\frac{\mathrm{i}\,q_z r^2}{2(z-z')}\right)\iint r'\,\mathrm{d}r'\,\mathrm{d}\phi'\,\mathrm{e}^{\mathrm{i}\,l\phi'}\exp\left[\mathrm{i}\,q_z\frac{-rr'\cos(\phi-\phi')}{z-z'}\right]. \quad (1.16)$$

As shown in Appendix A.5, the integral in ϕ' can be solved analytically and we are left with

$$\psi_l(r,\phi,z) = -\,\mathrm{i}\,q_z \frac{\mathrm{i}^l\,\psi_0}{z-z'} \exp\left(\frac{\mathrm{i}\,q_z r^2}{2(z-z')}\right) \mathrm{e}^{\mathrm{i}\,l\,\phi} \int_0^R r'\,\mathrm{d}r'\,J_l\left(-q_z \frac{r\,r'}{z-z'}\right), \tag{1.17}$$

where R is the radius of an aperture. From similar triangles, we can find that

$$q_{r'} = \frac{q_z\,r'}{z-z'} \tag{1.18}$$

and the last integration can be performed in the wavenumber $q_{r'}$ domain.

1.1.2 Practical Methotds of VEB preparation

Following section will show that previous theoretical assumptions are reasonable to make since real "phase plates" with transmission functions similar to those we have postulated above are practically well–achievable.

Several methods of VEB preparation have been demonstrated. The first to prepare VEB intentionally were Uchida and Tonomura in 2010 [16]. They have used graphite from a pencil in which they found structures with thickness singularity in the middle. As the Electron penetrates the material of varying thickness, it is delayed proportionally to the thickness and a vortex can be formed. This however is not very practical way of vortex preparation.

To measure if they really have prepared the vortices, they have used electron holography. From it a typical "fork" pattern arises, as is shown in Fig. 1.2b. We can reverse this process and let plane wave impinge on a diffraction grating prepared in the shape of the fork (Fig. 1.2c) using focused ion beam (FIB) lithography. This way, we can create vortices of opposite topological charges diverted from the main beam as is shown in Fig. 1.2d [19]. These holograms can be computer–computed and prepared for higher topological charges and used also as OAM filter by diverting the chosen vortex in a specific angle.

Spiral zone plates are simmilar in the production method (FIB) to the fork phase plates. They take shape shown in Fig. 1.2e. [18, 14] Today, even more sophisticated patterns are being used for measuring of sorting vortex states. Such phase plate as shown in [11] could be used as the proposed OAM filter in our experiment.

Vorticity can also be imprinted into the beam by EM field from surface plasmon polaritons generated by eliptically polarized LASER beam illuminating a circular slit in metal. [17]

One of promising designs of programmable phase plates for preparation of vortex (or other phase-tailored) electrons is an array of microscopic electrodes which can take form of einzel lenses. Depending on the potential profile forced on the electrodes, phase of the electron wave is delayed differently in different parts of the beam and vortex can be formed from plane wave. [21]

Add my figures if there is time. MAybe add figures from the articles.

More complicated designs of electronic devices enabling the preparation of VE with topological charge as high as 1000 have been showed [15].

1.2 Inelastic Interaction of VEB with Point-like Polarizable Particle

In this section, we will build on the wave function of the vortex electron beam (VEB) we have prepared earlier and derive an expression for electron energy loss spectrum (or spectral

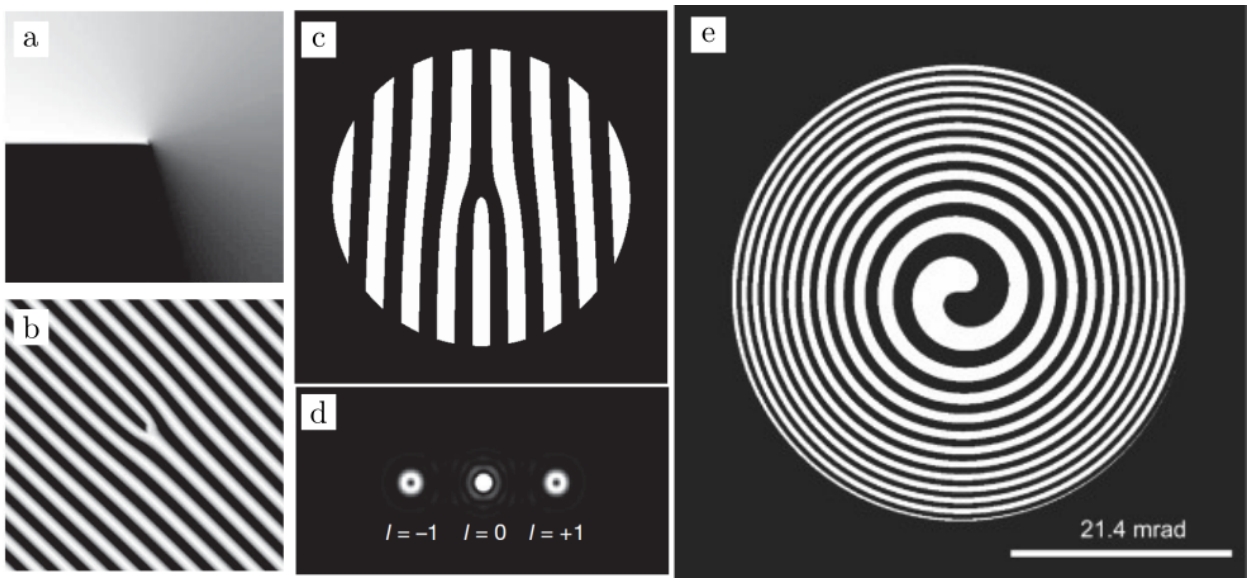

Figure 1.2: Measurement and Preparation of VEBs, Uchida [16] (a,b) and Verbeeck [19, 18] (c,d,e). a) phase profile of an ideal vortex. b) "fork" – hologram formed by interference of $l = 1$ vortex with plane wave. c) "fork" used by Verbeeck to prepare VEBs. d) profile of the beam generated by Verbeeck with difraction fork in (c). e) spiral zone plate for VEB preparation.

function EELSF) between two vortex states.

1.2.1 Modelled experiment setup

The setup of modelled experiment is captured in Fig. 1.3. VEBs prepared in the beam shaper interact with the specimen and can lose energy and sometimes OAM, which leads to a change of topological charge of the electron. The interaction mechanism is more precisely discussed in Sec. 2.1. After the interaction, the electron is in a superposition of all possible states. From those, one particular vortex state is chosen with OAM sorter. EELS is then measured for concrete topological charge transition $l_\mathrm{i} \to l_\mathrm{f}$.

1.2.2 Energy Loss Probability Spectrum

Below we present a model based on Fermi's golden rule based on first order perturbation theory. Subsequent paragraphs follow the references [10, 1].

We will work in the space of cylindrical coordinates (r, ϕ, z), see App. A.4. The non-relativistic wave function of VEB with topological charge l can be expressed as a function ψ_l of form

$$\psi_l(r, \phi, z) = \frac{1}{\sqrt{L}} \mathrm{e}^{\mathrm{i}\, q_z z}\, \psi_{l,\perp}(r, \phi). \tag{1.19}$$

Here, we have expressed the function as a product of two independent functions. The first being z–dependent phase factor dependent on wave vector's z component $q_z = m_e v/\hbar$ (here expressed as the product of electron's mass m_e and velocity v divided by reduced Planck's constant $\hbar$) with normalization prefactor dependent on normalization length L. The second

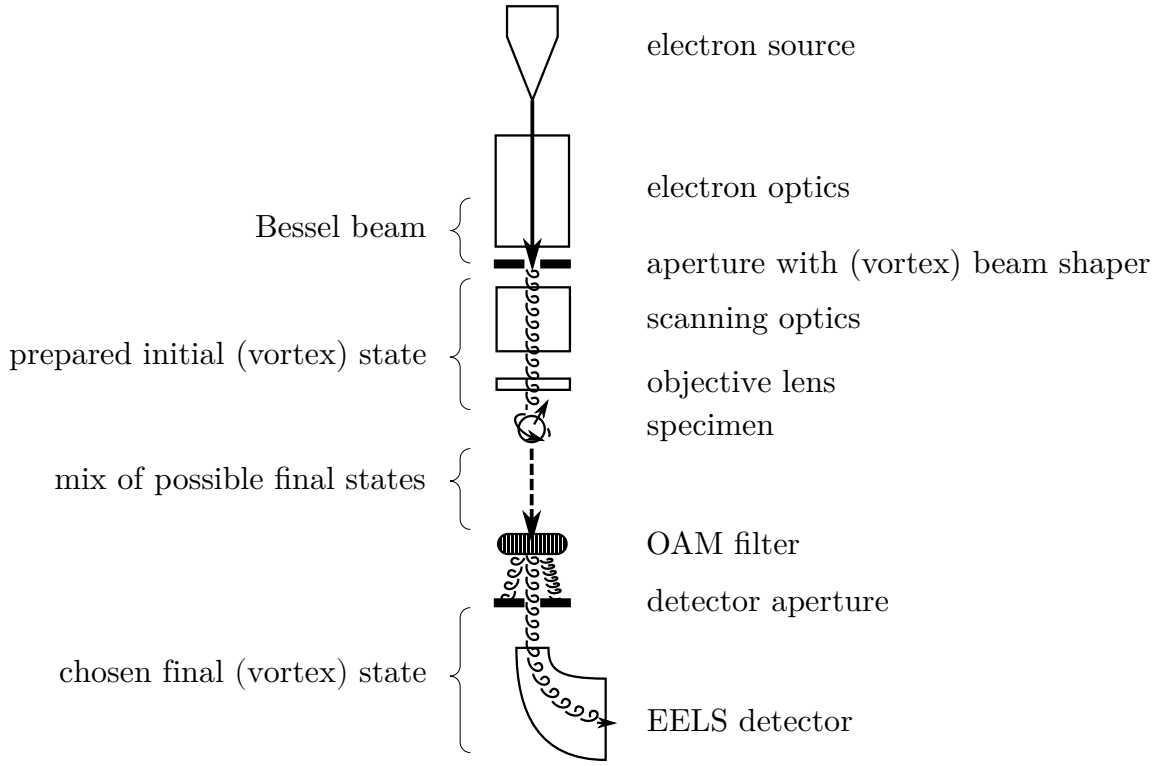

Figure 1.3: Simple scheme of modeled experiment. Electrons from electron cathode are accelerated to the desired eneregy and monochromated (monochromator is not shown in the figure). Traveling through series of optical elements, electrons reach an aperture with beam shaper (phase plate) and electron vortex is formed. This electron vortex is projecteted onto the specimen and interacts with it. With possible use of subsequent optics (not shown), the beam hits an OAM filter which spearetes a chosen vortex state from the mix emerging from the interaction with specimen. Finaly the electrons are measured by EELS.

function can be further broken down as

$$\psi_{l,\perp}(r,\phi) = \frac{1}{\sqrt{A}}\,\mathrm{e}^{\mathrm{i}\,l\phi}\,J_l(q_r r), \tag{1.20}$$

where normalization prefactor is dependent on normalization area A and J_l is Bessel function dependent on radial wavevector q_r. The Bessel function is responsible for the radial shape of the vortex. Its phase in the angular direction, i.e. its helicity, is governed by the exponential term $\exp(\mathrm{i}\,l\phi)$.

Such wavefunction can not be normalized through infinite space, however, similar reasoning as we have discussed below the Eq. (1.5) can be used. Set of these functions for $l \in \mathbb{Z}$ forms a complete basis of possible wavefunctions with such cylindrical symmetry.[1]

It can be shown that Eq. (1.19) is a solution of the Shrődinger equation for a free electron moving along z axis with the static orbital angular momentum (OAM) of magnitude $l\hbar$.

When electron with initial energy $\hbar\epsilon_\mathrm{i}$ (where ϵ_i is frequency corresponding to the energy) interacts with the specimen, photon of frequency ω transfers energy $\hbar\omega$ from electron to the

[1] As we have mentioned earlier, it is possible to use Laguerre functions. In our calculations, however, Bessel functions are sufficient enough and easy to work with.

specimen leaving the electron with final energy $\hbar\epsilon_\mathrm{f}$. Rate of transition from initial state ψ_i characterized by well defined initial energy to final state ψ_f can be expressed from first order perturbation theory, according to Fermi's Golden Rule, as [3]

$$\frac{\mathrm{d}\Gamma_{\mathrm{i}\to\mathrm{f}}}{\mathrm{d}t} = \frac{2\hbar e^2}{\omega^2 m^2} \int \mathrm{d}^3\mathbf{r}\,\mathrm{d}^3\mathbf{r}'\,\psi_\mathrm{f}(\mathbf{r})\,\psi_\mathrm{f}^*(\mathbf{r}')\,\nabla\left[\psi_\mathrm{i}^*(\mathbf{r})\right]\cdot\mathrm{Im}\left[\hat{\mathbf{G}}(\mathbf{r},\mathbf{r}',\omega)\right]\cdot\nabla\left[\psi_\mathrm{i}(\mathbf{r}')\right]\delta\left(\epsilon_\mathrm{f}-\epsilon_\mathrm{i}+\omega\right), \tag{1.21}$$

where $\hat{\mathbf{G}}$ is the Green's electromagnetic response tensor of the specimen. We are able to use this equation only if it is possible to construct the Green's tensor of response $\hat{\mathbf{G}}$. For point-like particle (for which homogeneous field in its vicinity is considered) the response tensor is discussed in Sec. 2.1.

Consider now an initial state in the form $\psi_\mathrm{i} = \exp(\mathrm{i}\,q_{z,\mathrm{i}}z)\psi_{\perp,\mathrm{i}}/\sqrt{L}$ and final state $\psi_\mathrm{f} = \exp(\mathrm{i}\,q_{z,\mathrm{f}}z)\psi_{\perp,\mathrm{f}}/\sqrt{L}$. By $\mathbf{r}_\perp$ we denote the z–perpendicular component of position vector. We have also used notation in which gradient $\nabla = [\nabla_\perp;\partial_z]$, where $\nabla_\perp = [\partial_x;\partial_y]$. After substitution of preceding terms into (1.21), we get

$$\begin{aligned}\frac{\mathrm{d}\Gamma_{\mathrm{i}\to\mathrm{f}}}{\mathrm{d}t} =& \frac{2\hbar e^2}{L^2\omega^2 m^2}\int \mathrm{d}^3\mathbf{r}\,\mathrm{d}^3\mathbf{r}'\,\mathrm{e}^{\mathrm{i}\,q_{z,\mathrm{f}}z}\psi_{\mathrm{f},\perp}(\mathbf{r}_\perp)\,\mathrm{e}^{-\mathrm{i}\,q_{z,\mathrm{f}}z'}\,\psi_{\mathrm{f},\perp}^*(\mathbf{r}_\perp{}')\\ &\times \mathrm{e}^{-\mathrm{i}\,q_{z,\mathrm{i}}z}\left[\nabla_\perp\left\{\psi_{\mathrm{i},\perp}^*(\mathbf{r}_\perp)\right\};-\mathrm{i}\,q_{z,\mathrm{i}}\psi_{\mathrm{i},\perp}^*(\mathbf{r}_\perp)\right]\cdot\mathrm{Im}\left[\hat{\mathbf{G}}(\mathbf{r},\mathbf{r}',\omega)\right]\cdot\\ &\times \mathrm{e}^{\mathrm{i}\,q_{z,\mathrm{i}}z'}\left[\nabla_\perp\left\{\psi_{\mathrm{i},\perp}(\mathbf{r}'_\perp)\right\};\mathrm{i}\,q_{z,\mathrm{i}}\psi_{\mathrm{i},\perp}(\mathbf{r}'_\perp)\right]\delta\left(\epsilon_f-\epsilon_i+\omega\right) =\\ =& \frac{2\hbar e^2}{L^2\omega^2 m^2}\int \mathrm{d}^3\mathbf{r}\,\mathrm{d}^3\mathbf{r}'\,\mathrm{e}^{\mathrm{i}(z-z')(q_{z,\mathrm{f}}-q_{z,\mathrm{i}})}\delta\left(\epsilon_f-\epsilon_i+\omega\right)\,\psi_{\mathrm{f},\perp}(\mathbf{r}_\perp)\,\psi_{\mathrm{f},\perp}^*(\mathbf{r}_\perp{}')\\ &\times\left[\nabla_\perp\left\{\psi_{\mathrm{i},\perp}^*(\mathbf{r}_\perp)\right\};-\mathrm{i}\,q_{z,\mathrm{i}}\psi_{\mathrm{i},\perp}^*(\mathbf{r}_\perp)\right]\cdot\mathrm{Im}\left[\hat{\mathbf{G}}(\mathbf{r},\mathbf{r}',\omega)\right]\cdot\left[\nabla_\perp\left\{\psi_{\mathrm{i},\perp}(\mathbf{r}'_\perp)\right\};\mathrm{i}\,q_{z,\mathrm{i}}\psi_{\mathrm{i},\perp}(\mathbf{r}'_\perp)\right].\end{aligned} \tag{1.22}$$

Now we will express the energy loss probability for given energy (frequency w). The time T it takes one electron to move along path of length L on the z axis with speed v is $T = L/v$. Since our previous expression describes the (time) rate of electron transition from well–defined initial state to concrete final state, to get the overall probability of electron transitioning to any of the final states we will need to sum through all the possible final states and multiply the rate of transition by the electron–specimen interaction time (see above). From there we get the loss probability spectrum function:

$$\Gamma(\omega) = \frac{L}{v}\sum_\mathrm{f}\frac{\mathrm{d}\Gamma_{\mathrm{i}\to\mathrm{f}}}{\mathrm{d}t}. \tag{1.23}$$

The sum of all states can be replaced by integral through all the wavevectors. Lower, we divided the sum to one which sums through the perpendicular part of wavevector and other (rewritten as integral) for the z–axis part. We further need a prefactor $L/2\pi$ converting the wave vector $q_{z,\mathrm{f}}$ to its corresponding frequency ϵ_f. Symbolicaly written: $\sum_\mathrm{f} \to \sum_{\mathrm{f},\perp}\int \mathrm{d}q_z L/2\pi$.

$$\Gamma(\omega) = \frac{L}{v}\sum_{\mathrm{f},\perp}\int \mathrm{d}q_{z,\mathrm{f}}\frac{L}{2\pi}\frac{\mathrm{d}\Gamma_{\mathrm{i}\to\mathrm{f}}}{\mathrm{d}t}. \tag{1.24}$$

We now expand this expression and get

$$\Gamma(\omega) = \frac{\hbar e^2}{v\omega^2\pi m^2} \int \mathrm{d}^3\mathbf{r}\,\mathrm{d}^3\mathbf{r}' \sum_{\mathrm{f},\perp} \int \mathrm{d}q_{z,\mathrm{f}}\, \mathrm{e}^{\mathrm{i}(z-z')(q_{z,\mathrm{f}}-q_{z,\mathrm{i}})}\, \delta\left(\epsilon_f - \epsilon_i + \omega\right)\, \psi_{\mathrm{f},\perp}(\mathbf{r}_\perp)\, \psi^*_{\mathrm{f},\perp}(\mathbf{r}_\perp{}') \times \left[\nabla_\perp \left\{\psi^*_{\mathrm{i},\perp}(\mathbf{r}_\perp)\right\}; -\mathrm{i}\, q_{z,\mathrm{i}}\psi^*_{\mathrm{i},\perp}(\mathbf{r}_\perp)\right] \cdot \mathrm{Im}\left[\hat{\mathbf{G}}(\mathbf{r},\mathbf{r}',\omega)\right] \cdot \left[\nabla_\perp \left\{\psi_{\mathrm{i},\perp}(\mathbf{r}'_\perp)\right\}; \mathrm{i}\, q_{z,\mathrm{i}}\psi_{\mathrm{i},\perp}(\mathbf{r}'_\perp)\right] \tag{1.25}$$

Let's focus on the innermost integral of the previous expression for now.

$$\int \mathrm{d}q_{z,\mathrm{f}}\, \mathrm{e}^{\mathrm{i}(z-z')(q_{z,\mathrm{f}}-q_{z,\mathrm{i}})}\, \delta\left(\epsilon_f - \epsilon_i + \omega\right)$$

Energy and momentum of a particle are closely related. If we write energy expressed in terms of momentum $p = \hbar q$ on one side of an equation and in terms of its frequency ϵ on the other side, we get

$$\frac{(\hbar q)^2}{2m} = \hbar\epsilon, \tag{1.26}$$

thus frequency can be expressed as

$$\epsilon = \frac{\hbar q^2}{2m}. \tag{1.27}$$

We will now assume that most of the electron's energy is bound in the movement along z axis. Thus we will be able to express all of the energy–related frequencies in terms of z components of wavevectors. In other words, we will use paraxial (or non–recoil) approximation. Because of the filtering property of Dirac's delta δ, the result of the integral is the integrand in which we substitute for the integrated varible the value, in which the argument of δ is equal to zero. Using previous expression, we get

$$\begin{aligned} 0 &= \frac{\hbar q_{\mathrm{f}}^2}{2m} - \frac{\hbar q_{\mathrm{i}}^2}{2m} + \omega, \\ q_{\mathrm{f}} &= q_{\mathrm{i}}\sqrt{1 - \frac{2m}{\hbar q_{\mathrm{i}}^2}\omega} \approx \\ &\approx q_{\mathrm{i}}\left(1 - \frac{m}{\hbar q_{\mathrm{i}}^2}\omega\right). \end{aligned} \tag{1.28}$$

The z subscripts were intentionally left out for clarity. In the last step we have assumed that $\omega \ll \epsilon_i$ and the square root approximation rule (see A.3) was used. This is a very plausible step, since the swift electron loses typically only fraction of order lower than 10^{-3} of its initial energy interacting with the specimen [1, p. 213].

Expanding the last term with momentum $\hbar q_i = p = mv$ we get

$$q_{\mathrm{f}} = q_{\mathrm{i}}\left(1 - \frac{\omega}{vq_{\mathrm{i}}}\right). \tag{1.29}$$

Further, we substitute (from eq. (1.27)) for $\mathrm{d}q_{z,\mathrm{f}} = \mathrm{d}\epsilon_{\mathrm{f}} m/\hbar q_{z,\mathrm{f}} = \mathrm{d}\epsilon_{\mathrm{f}}/v$. Altogether we get

$$\int \mathrm{d}q_{z,\mathrm{f}}\, \mathrm{e}^{\mathrm{i}(z-z')(q_{z,\mathrm{f}}-q_{z,\mathrm{i}})}\, \delta\left(\epsilon_f - \epsilon_i + \omega\right) = \frac{1}{v}\exp\left(-\mathrm{i}\,\omega\frac{z-z'}{v}\right). \tag{1.30}$$

By substituting this integral into Eq. (1.25) we get

$$\Gamma(\omega) = \frac{\hbar e^2}{v\omega^2\pi m^2}\int \mathrm{d}^3\mathbf{r}\,\mathrm{d}^3\mathbf{r}'\,\frac{1}{v}\exp\left(-\mathrm{i}\,\omega\frac{z-z'}{v}\right)\sum_{\mathrm{f},\perp}\psi_{\mathrm{f},\perp}(\mathbf{r}_\perp)\,\psi^*_{\mathrm{f},\perp}(\mathbf{r}_\perp{}') \times\left[\nabla_\perp\left\{\psi^*_{\mathrm{i},\perp}(\mathbf{r}_\perp)\right\};-\mathrm{i}\,q_{z,\mathrm{i}}\psi^*_{\mathrm{i},\perp}(\mathbf{r}_\perp)\right]\cdot\mathrm{Im}\left[\hat{\mathbf{G}}(\mathbf{r},\mathbf{r}',\omega)\right]\cdot\left[\nabla_\perp\left\{\psi_{\mathrm{i},\perp}(\mathbf{r}'_\perp)\right\};\mathrm{i}\,q_{z,\mathrm{i}}\psi_{\mathrm{i},\perp}(\mathbf{r}'_\perp)\right] \tag{1.31}$$

For further simplification, we define

$$\hat{\mathcal{G}}(\mathbf{r}_\perp,\mathbf{r}'_\perp,\omega) = \int \mathrm{d}z\,\mathrm{d}z'\exp\left(-\mathrm{i}\,\omega\frac{z-z'}{v}\right)\mathrm{Im}\left[\hat{\mathbf{G}}(\mathbf{r},\mathbf{r}',\omega)\right] \tag{1.32}$$

and substitute this into the Eq. (1.31); we get

$$\Gamma(\omega) = \frac{\hbar e^2}{v^2\omega^2\pi m^2}\int \mathrm{d}^2\mathbf{r}_\perp\,\mathrm{d}^2\mathbf{r}'_\perp\,\sum_{\mathrm{f},\perp}\psi_{\mathrm{f},\perp}(\mathbf{r}_\perp)\,\psi^*_{\mathrm{f},\perp}(\mathbf{r}_\perp{}') \times\left[\nabla_\perp\left\{\psi^*_{\mathrm{i},\perp}(\mathbf{r}_\perp)\right\};-\mathrm{i}\,q_{z,\mathrm{i}}\psi^*_{\mathrm{i},\perp}(\mathbf{r}_\perp)\right]\cdot\hat{\mathcal{G}}(\mathbf{r}_\perp,\mathbf{r}'_\perp,\omega)\cdot\left[\nabla_\perp\left\{\psi_{\mathrm{i},\perp}(\mathbf{r}'_\perp)\right\};\mathrm{i}\,q_{z,\mathrm{i}}\psi_{\mathrm{i},\perp}(\mathbf{r}'_\perp)\right]. \tag{1.33}$$

For the sum in the last expression, we can again move from discrete to continuous domain. Now, it is time to decide, whether it will be best to work in Cartesian or in radial coordinates. This depends on the form of wave and the type of detector i.e. their symmetries. If the detector was square or the wave was of any arbitrary (radially non-symmetric) shape, we shall use Cartesian coordinates and integrate over the detector's q-space.

$$\sum_{\mathrm{f},\perp}\to\frac{A}{(2\pi)^2}\int\mathrm{d}q_{\mathrm{f},x}\int\mathrm{d}q_{\mathrm{f},y}. \tag{1.34}$$

As the basis for the space of wave functions $\psi_\perp$, we can then use a set of functions of the form

$$\psi_\perp^{(q_x,q_y)} = \frac{1}{\sqrt{A}}\exp\left[\mathrm{i}(q_x\,x+q_y\,y)\right], \tag{1.35}$$

where A is a normalization constant.

The spectral loss function then becomes

$$\Gamma(\omega) = \frac{\hbar e^2}{v^2\omega^2\pi m^2}\int\mathrm{d}x\,\mathrm{d}y\,\mathrm{d}x'\,\mathrm{d}y'\,\frac{A}{(2\pi)^2}\int\mathrm{d}q_{\mathrm{f},x}\mathrm{e}^{\mathrm{i}\,q_{\mathrm{f},x}(x-x')}\int\mathrm{d}q_{\mathrm{f},y}\mathrm{e}^{\mathrm{i}\,q_{\mathrm{f},y}(y-y')} \left[\nabla_\perp\left\{\psi^*_{\mathrm{i},\perp}(x,y)\right\};-\mathrm{i}\,q_{z,\mathrm{i}}\psi^*_{\mathrm{i},\perp}(x,y)\right]\cdot\hat{\mathcal{G}}(x,y,x',y',\omega)\cdot\left[\nabla_\perp\left\{\psi_{\mathrm{i},\perp}(x',y')\right\};\mathrm{i}\,q_{z,\mathrm{i}}\psi_{\mathrm{i},\perp}(x',y')\right]. \tag{1.36}$$

If there exists radial symmetry in the problem, however, it might be better to use radial coordinates. In our case (when studying VEBs) it is convenient to use a basis of functions of form (1.19). These hold the vorticity of the beam naturally and can be expressed as

$$\psi_{\mathrm{f},\perp}(r,\phi) = \frac{1}{\sqrt{A}}\,\mathrm{e}^{\mathrm{i}\,l_\mathrm{f}\phi}\,J_l(q_{\mathrm{f},r}r), \tag{1.37}$$

To move from discrete to continuous domain, we can write

$$\sum_{\mathrm{f},\perp} \to \frac{A}{(2\pi)^2} \int_0^{Q_c} q_{\mathrm{f},r} \mathrm{d}q_{\mathrm{f},r} \int_0^{2\pi} \mathrm{d}q_{\mathrm{f},\phi} \sum_{l_\mathrm{f}} = \frac{A}{2\pi} \int_0^{Q_c} q_{\mathrm{f},r} \mathrm{d}q_{\mathrm{f},r} \sum_{l_\mathrm{f}}, \tag{1.38}$$

where we can evaluate the second integral since used basis functions are $q_{\mathrm{f},\phi}$–independent.

When the OAM sorter is used, only one basis function corresponding to the concrete chosen l_f is then needed to describe the final state. and we can leave out the sum over all possible l_fs. Loss probability spectrum for the chosen l_f is then

$$\begin{aligned}\Gamma_{l_\mathrm{f}}(\omega) =& \frac{\hbar e^2}{2\pi^2 v^2 \omega^2 m^2} \int \mathrm{d}^2\mathbf{r}_\perp \, \mathrm{d}^2\mathbf{r}'_\perp \, \mathrm{e}^{\mathrm{i}\, l_\mathrm{f}(\phi-\phi')} \int_0^{Q_c} q_{\mathrm{f},r} \, \mathrm{d}q_{\mathrm{f},r} \; J_l(q_{\mathrm{f},r} r) \, J_l(q_{\mathrm{f},r} r') \\ & \times \left[\nabla_\perp \left\{\psi^*_{\mathrm{i},\perp}(\mathbf{r}_\perp)\right\}; -\mathrm{i}\, q_{z,\mathrm{i}} \psi^*_{\mathrm{i},\perp}(\mathbf{r}_\perp)\right] \cdot \hat{\mathcal{G}}(\mathbf{r}_\perp, \mathbf{r}'_\perp, \omega) \cdot \left[\nabla_\perp \left\{\psi_{\mathrm{i},\perp}(\mathbf{r}'_\perp)\right\}; \mathrm{i}\, q_{z,\mathrm{i}} \psi_{\mathrm{i},\perp}(\mathbf{r}'_\perp)\right].\end{aligned} \tag{1.39}$$

This is the final expression for the energy loss spectral function (EELSF).[2] It describes the probability density (upon range of photon frequencies ω) of electron losing energy $\hbar\omega$ if we know, that after interaction with the specimen the electron had left with final topological charge l_f. If more states with different topological charges from the set $\{l_\mathrm{f}\}$ are needed, the spectral loss function for those states would be a simple sum

$$\Gamma_{\{l_\mathrm{f}\}}(\omega) = \sum_{l \in \{l_\mathrm{f}\}} \Gamma_l(\omega). \tag{1.40}$$

1.3 About Electron Energy Loss Spectroscopy

In the previous section we have derived an Electron Energy Loss Spectrum (EELSF) for electron moving in the vicinity of a polarizable particle. Now we shall examine Electron Energy Loss Spectroscopy (EELS) in a fast overview.

The result of EELS measurement is electron energy loss spectrum (spectral function, EELSF) denoted Γ.

Electron moving in the vicinity of a specimen (5 nm from it) with energy 30 keV generates changing electromagnetic field of frequencies ranging 0 eV–30 eV. That means it acts as a broadband source of optical radiation. [13]

The basic principle of EELS is the Law of conservation of energy. If we measure that the electron interacting with a specimen lost some defined energy $\hbar\omega$, we immediately know that the specimen must have gained the same amount of energy $\hbar\omega$ from the interaction.

García de Abajo and Kociak showed in [8] that in the case of geometries where translational invariance in the direction of the beam exists the EELS spectrum is proportional to the local density of optical states (LDOS) enabling us to map optical excitations directly. For more general geometries this may not hold true, however in many cases it (at least qualitatively) does.

EELS maps the specimen by interaction in near-field so the spatial resolution is mainly limited by the span of the evanescent field of the electron. Thanks to the near-field interaction, we are not bound to radiative losses in the specimens. The fact that EELS maps all

[2] However, we do not use this exact Exp. to calculate our semianalytical spectra. See Sec. 2.1, precisely Expr. (2.18) for further explanation.

excitaitions is a big advantage in comparison to CL which accounts only for radiative losses, thus generally $\Gamma_{\mathrm{EELS}} \geq \Gamma_{\mathrm{CL}}$.

EELS can be used to probe plasmons since 2007 [6]. Today even plasmon tomography is possible [13]. EELS can be angle-resolved which enables us to study structures with translational symmetries in inverse space rather than in real. The energy resolution in some setups has already lowered under 10 meV and we are able to analyze energies > 30 meV, which enables us to study even phonons.

To model an interaction with a real sample, one usually has to numerically solve Maxwell's equations. Several methods are known. One of them is Boundary Element Method (BEM), which is further discussed in chapter [XXX]. In some cases, as is ours for the point-like particle in Sec. [XXX], we can bypass the numerical solution.

When the specimen is excited before (or together) with the interaction with the specimen, it can also give the energy to (not take it from) the electron. When this phenomenon is measured in spectra, we talk about Elelctron Energy Gain Spectroscopy (EEGS)

Temporal infromation about the interaction with the specimen can be gained from Fourier analysis of the measured data.

zero loss peak

Structured beams in EELS

As we have already discussed in the Sec. 1.1 the wavefunctions of electrons can be tailored in multifarious ways (for example with programmable phase plates (PPPs)). This introduces new degrees of freedom which can be used to study more phenomena in a more simple and faster measurement or even open new fields of study for example in the study of magnetic structers or chiral substances or materials which are very common in nature. Beams structured in spatial or temporal domains can be viewed as "quantum probes" which can reveal all kinds of new information about specimen, since after the interaction the electron's state is entangled with the specimen's. This enables us to analyze the state of electons byand gain information about the state of specimens. This can open new fields in microscopy. Last but not least, the use of structured electron beams can reduce the need for correctors and reduce the complexity of electron microscopes column. Thus TEMs could become smaller.

Chapter 2

Semi–Analytical Model of VEB's Interaction with chiral point object

2.1 Green's Response Tensor

In this section we will discus the Green's response tensor needed for evaluation of EEL spectral function derived in Sec. 1.2.

For the next couple of paragraphs we roughly follow [12]. Helmholtz Eq. for electromagnetic field in the domain of frequencies ω with corresponding wavenumber $k = \omega/c$ (where c is the speed of light) in vacuum with Lorenz gauge can be written in the following form for 4-potential A^i (thus for classical vector and scalar potentials) and 4-current J^i as

$$\left[\nabla^2 + k^2\right] A^i = -\mu_0 J^i. \tag{2.1}$$

Focus now on any one component. Assuming the charge density (or one particular component of current density) to be concentrated in one concrete (source) point $\mathbf{r}'$ so that the total charge (current) is unit, we can rewrite previous expression for any (field) point $\mathbf{r}$ in space using Dirac's delta as

$$\left[\nabla^2 + k^2\right] G_0(\mathbf{r}, \mathbf{r}') = -\delta(\mathbf{r} - \mathbf{r}'), \tag{2.2}$$

where $G_0(\mathbf{r}, \mathbf{r}')$ is some function. Since the Helmholtz operator is linear there exists (in general) an inverse operator (traditionally called green's operator) which acts as a response operator on the unit impulse. If this operator is known, we can then find the response for any possible impulse. In our case we can find the potential field $A^i(\mathbf{r})$ in any point in space for any possible current density field $J^i(\mathbf{r})$ as

$$A^i(\mathbf{r}) = \underbrace{\int \mathrm{d}^3\mathbf{r}'\, \mu_0\, G_0(\mathbf{r}, \mathbf{r}')}\; J^i(\mathbf{r}'), \tag{2.3}$$

where we have underbraced the mentioned linear operator.

Function $G_0(\mathbf{r}, \mathbf{r}')$ known as scalar vacuum Green's function can be found for the 3D Helmholtz equation in the form

$$G_0(\mathbf{r}, \mathbf{r}') = \frac{\exp\left(\mathrm{i}\, k|\mathbf{r} - \mathbf{r}'|\right)}{4\pi|\mathbf{r} - \mathbf{r}'|}. \tag{2.4}$$

We can see that the expression is dependent only on the difference between $\mathbf{r}$ and $\mathbf{r}'$, thus it is possible to write $G_0(\mathbf{r}, \mathbf{r}') = G_0(\mathbf{r} - \mathbf{r}')$.

Similarly, the Green operator can be found for electric $\mathbf{E}$ and magnetic $\mathbf{H}$ fields. Since those are 3-component vector quantities the Green's operator must be a tensor of rank 3.

$$\mathbf{E}(\mathbf{r}) = \frac{\mathrm{i}}{\omega} \int \mathrm{d}^3\mathbf{r}'\, \hat{\mathbf{G}}_{\mathrm{EE}}(\mathbf{r}, \mathbf{r}') \cdot \mathbf{J}(\mathbf{r}'), \tag{2.5}$$

??? $$\mathbf{H}(\mathbf{r}) = \int \mathrm{d}^3\mathbf{r}'\, \hat{\mathbf{G}}_{\mathrm{ME}}(\mathbf{r}, \mathbf{r}') \cdot \mathbf{J}(\mathbf{r}'). \tag{2.6}$$

The current density $\mathbf{J}$ can be further calculated from dipole moment $\mathbf{p}$ as

$$\mathbf{J}(\mathbf{r}') = -\,\mathrm{i}\,\omega\,\mathbf{p}\,\delta(\mathbf{r}' - \mathbf{r_0}), \tag{2.7}$$

where $\mathbf{r}_0$ is the position of the dipole.

The Green's dyadic electro-electric function $\hat{\mathbf{G}}_{\mathrm{EE}}$ can be calculated from the scalar vacuum Green's function G_0 as

$$\hat{\mathbf{G}}_{\mathrm{EE}}(\mathbf{r}, \mathbf{r}') = \frac{1}{\varepsilon_0} \left[k^2 \hat{\mathbf{1}} + \nabla' \otimes \nabla'\right] G_0(\mathbf{r}, \mathbf{r}'), \tag{2.8}$$

where $\hat{\mathbf{1}}$ is unit operator, ∇' is the nabla operator in respect to primed (source) position vector $\mathbf{r}'$ and $\otimes$ stands for tensor product. The Green's dyadic electro-magnetic function $\hat{\mathbf{G}}_{\mathrm{ME}}$ is then

$$\hat{\mathbf{G}}_{\mathrm{ME}}(\mathbf{r}, \mathbf{r}') = \frac{1}{\mathrm{i}\,\omega} \nabla' \times \hat{\mathbf{G}}_{\mathrm{EE}}(\mathbf{r}, \mathbf{r}'). \tag{2.9}$$

It describes the magnetic field induced by electrical current (dipole).

From the symmetry of Maxwell's Eqs. [10] it can be shown that Green's magneto-magnetic tensor

$$\hat{\mathbf{G}}_{\mathrm{MM}} = \hat{\mathbf{G}}_{\mathrm{EE}} \tag{2.10}$$

and Green's magneto-electric tensor

$$\hat{\mathbf{G}}_{\mathrm{EM}} = -\hat{\mathbf{G}}_{\mathrm{ME}}. \tag{2.11}$$

In the Eq. (1.32) we have defined (following [10]) a Green's response tensor integrated along z axes. To fully construct it, we will define

$$\begin{aligned} \hat{\mathbf{G}}^{\mathrm{int}}_{\mathrm{EE}}(\mathbf{r}, \mathbf{r}') &= \int \mathrm{d}z\, \mathrm{d}z'\, \exp\left(-\,\mathrm{i}\,\omega \frac{z - z'}{v}\right) \hat{\mathbf{G}}_{\mathrm{EE}} = \\ &= \frac{1}{2\pi\varepsilon_0} (k^2 \hat{\mathbf{1}} + \nabla' \otimes \nabla') \left[\mathrm{e}^{\,\mathrm{i}\,\omega \frac{z_\mathrm{p}}{v}} K_0\left(\frac{\omega |\mathbf{r}_\perp - \mathbf{r}'_\perp|^2}{v\,\gamma_\mathrm{L}}\right)\right], \end{aligned} \tag{2.12}$$

where K_0 is modified Bessel's function of order 0, $\gamma_\mathrm{L} = 1/\sqrt{1 - v^2/c^2}$ is Lorentz factor.

Thanks to the linearity of differential operators used in derivation of dyadic functions from vacuum Green function, previously stated relations between different Green's tensors are retained for their integrated forms:

$$\hat{\mathbf{G}}^{\mathrm{int}}_{\mathrm{EM}}(\mathbf{r}, \mathbf{r}') = -\frac{1}{\mathrm{i}\,kc} \nabla' \times \hat{\mathbf{G}}^{\mathrm{int}}_{\mathrm{EE}}(\mathbf{r}, \mathbf{r}'), \tag{2.13}$$

$$\hat{\mathbf{G}}^{\mathrm{int}}_{\mathrm{MM}} = \hat{\mathbf{G}}^{\mathrm{int}}_{\mathrm{EE}}, \tag{2.14}$$

and

$$\hat{\mathbf{G}}^{\text{int}}_{\text{ME}} = -\hat{\mathbf{G}}^{\text{int}}_{\text{EM}}. \tag{2.15}$$

The electron moving in the chamber generates electric and magnetic field around the specimen. This is described by the Green's electro-electric and electro-magnetic tenzors. Assuming the specimen is small enough so the field around it is homogeneous we can describe it by simple polarizability tensors:

$$\begin{aligned} \text{electro-electric} \quad & \mathbf{E} \to \mathbf{p} \quad \hat{\alpha}_{\text{EE}}, \\ \text{electro-magnetic} \quad & \mathbf{E} \to \mu \quad \hat{\alpha}_{\text{ME}}, \\ \text{magneto-electric} \quad & \mathbf{H} \to \mathbf{p} \quad \hat{\alpha}_{\text{EM}}, \\ \text{electro-magnetic} \quad & \mathbf{H} \to \mu \quad \hat{\alpha}_{\text{MM}}. \end{aligned}$$

Again, thanks to the symmetry between electric a magnetic fields, we can write

$$\hat{\alpha}_{\text{ME}} = -\hat{\alpha}^{T}_{\text{EM}} \tag{2.16}$$

This induced electric (magnetic) dipole creates its own electric and magnetic field, which is captured, again, by Green's electro-electric and electro-magnetic (magneto-electric and magneto-magnetic) tenzors.

It is essential to mention, that if the specimen is polarizable in the crossed electric-magnetic terms $\hat{\alpha}_{\text{EM}}$ and $\hat{\alpha}_{\text{ME}}$, it must always be polarizable in the electric $\hat{\alpha}_{\text{EE}}$ and magnetic $\hat{\alpha}_{\text{MM}}$ terms. [3]

Magnetic field does not change the energy of the electron. We can also assume that the trajectory of the electron is almost unchanged by the magnetic field produced by the specimen. This means that we can neglect magnetic forces acting on the electron in our computations relating EELS. To capture the whole interaction of the electron with the specimen, we then define Green's response tensor

$$\check{\mathcal{G}}(\mathbf{r}, \mathbf{r}', \omega) = \check{\mathcal{G}}_{\text{EE}}(\mathbf{r}, \mathbf{r}', \omega) = \hat{\mathbf{G}}^{\text{int}}_{\text{E}i}(\mathbf{r}, \mathbf{r}_{\text{p}}, \omega) \cdot \hat{\alpha}_{ij}(\omega) \cdot \hat{\mathbf{G}}^{\text{int}}_{j\text{E}}(\mathbf{r}_{\text{p}}, \mathbf{r}', \omega), \tag{2.17}$$

where we have used Einstein summation rule (ESR) through indices $i, j \in \{\text{E}, \text{M}\}$ and $\mathbf{r}_{\text{p}}$ is the position of the studied particle (specimen). This tensor is in fact only electro-electric, as we have captured by the lower indices EE. However, since we don't need the magnetic ones we will omit the lower indices straight away. This is not yet the Green's response tensor defined in Expr. 2.17. However we were able to find the green response operator "without the imaginary part function" (compare Exprs. (1.32) and (2.12)). In the Expr. 1.39 the imaginary part is still inside the integrand. Fortunately, it can be pulled out [1] in front of the integral and EELSF can be calculated as

$$\begin{aligned} \Gamma_{l_{\text{i}} \to l_{\text{f}}}(\omega) = & \frac{\hbar e^2}{2\pi^2 v^2 \omega^2 m^2} \text{Im} \left\{ \int \text{d}^2\mathbf{r}_\perp \, \text{d}^2\mathbf{r}'_\perp \, \text{e}^{\,\text{i}\, l_{\text{f}}(\phi - \phi')} \int_0^{Q_c} q_{\text{f},r} \, \text{d}q_{\text{f},r} \; J_l(q_{\text{f},r} r) \, J_l(q_{\text{f},r} r') \right. \\ & \left. \times \left[\nabla_\perp \left\{ \psi^*_{\text{i},\perp}(\mathbf{r}_\perp) \right\} ; -\text{i}\, q_{z,\text{i}} \psi^*_{\text{i},\perp}(\mathbf{r}_\perp) \right] \cdot \check{\mathcal{G}}(\mathbf{r}_\perp, \mathbf{r}'_\perp, \omega) \cdot \left[\nabla_\perp \left\{ \psi_{\text{i},\perp}(\mathbf{r}'_\perp) \right\} ; \text{i}\, q_{z,\text{i}} \psi_{\text{i},\perp}(\mathbf{r}'_\perp) \right] \right\}. \end{aligned} \tag{2.18}$$

To grasp the interaction intuitively, a diagram of the interaction is shown in Fig. 2.1. Let's focus on this Figure now and explain intuitively what is happening. As we have already mentioned, Swift electron is a source of optical excitation thanks to its evanescent field. When a point-like particle is placed in the vicinity of the beam, it feels the field. We

have described the particle by 4 polarizability tensors. Two of them are "pure", $\hat{\alpha}_{\mathrm{EE}}$ and $\hat{\alpha}_{\mathrm{MM}}$, and two of them are "crossed". In our set-up we have another degree of freedom – distance between the specimen and the center of the vortex.

The pure terms account for achiral (or non-chiral) modes excited on the particle. The crossed terms are at play if the particle is chiral in nature (by material or structure). On such particle, chiral modes can be excited.

Any modes excited create their own field which acts back on the electron. This is how the electron loses its energy. After the interaction, the electron is in a superposition of all possible final states.

If not only the specimen is chiral but the electron impinging on it too, the symmetry breaks and dichroism emerges. In this context, dichroism is the effect of different response to qualitatively opposite impulses, the difference between response on right-hand vs left-hand vortex or, with the same initial topological charge l, the difference between positive $+\Delta l$ vs negative $-\Delta l$ change of topological charge in the interaction.

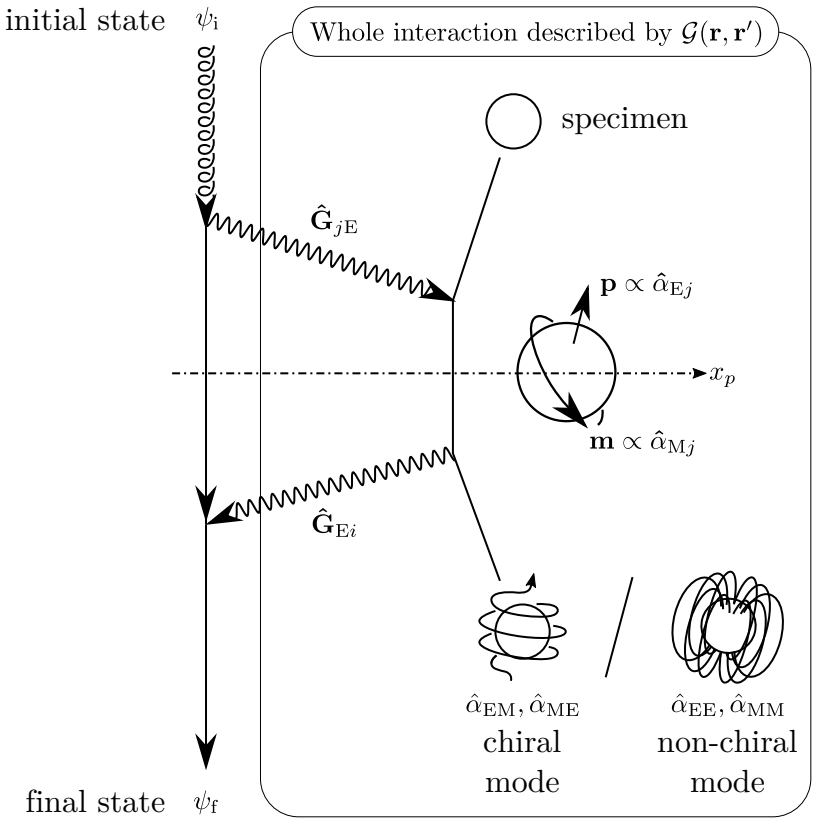

Figure 2.1: Diagram of the interaction of an electron with the specimen.

2.1.1 Drude Model for Relative Permitivity

Frequency dependent relative permitivities (dielectric functions) are usually tabulated. Some metals including silver (Ag) are well characterized by Drude free electron model which yields the relative permitivity

$$\varepsilon(\omega) = 1 - \frac{\omega_p^2}{\omega^2 + \mathrm{i}\,\gamma\omega}, \tag{2.19}$$

where ω_p is the bulk plasmon frequency of studied metal and γ is a small phenomenological relaxation rate which accounts for the dampening of plasma oscillation in the metal. In our calculation we have used universally the values $\hbar\omega_p = 9.1\,\mathrm{eV}$ and $\hbar\gamma = 0.15\,\mathrm{eV}$. [1]

2.1.2 Polarizability Tensor of a Sphere

Thanks to the total symmetry of a sphere, polarizability of a spherical metallic particle with radius a and relative permitivity $\varepsilon(\omega)$ can be described by scalar function $\alpha(\omega)$ as [3]

$$\alpha(\omega) = 4\pi\varepsilon_0 \frac{3\,c^3}{2\,\omega^3} \frac{-j_1(\rho_0)\,[\rho_1\,j_1(\rho_1)]' + \varepsilon(\omega) j_1(\rho_1)\,[\rho_0\,j_1(\rho_0)]'}{h_1^{(+)}(\rho_0)\,[\rho_1\,j_1(\rho_1)]' - \varepsilon(\omega) j_1(\rho_1)\,[\rho_0\,h_1^{(+)}(\rho_0)]'}, \tag{2.20}$$

where $j_1(x) = \sin(x)/x^2 - cos(x)/x$ and $h_1^{(+)}(x) = (1/x^2 - \mathrm{i}\,/x)\exp(\mathrm{i}\,x)$ are spherical Bessel and Hankel functions, respectively, prime stands for differentiation with respect to the argument and $\rho_0 = \omega\,a/c$ and $\rho_1 = \sqrt{\varepsilon(\omega)}\,\rho_0$. Said expression was used to gain realistic polarizability in our calculations, where we have used universally the value for radius $a = 5\,\mathrm{nm}$. Throughout our calculations we have universally assumend diagonal polarizability tensors wit equal values in each axis so that $\hat{\alpha}(\omega) = \alpha(\omega)\cdot\hat{\mathbf{1}}$. More complicated (non-diagonal) tensor would work too.

2.2 Implementation

This section will describe the implementation of calculations. After the derivation of expression for EELSF in Sec. 1.2 and derivation of Green's response tensor in Sec. 2.1 we could implement those into a computer program to calculate the spectra. We have chosen programming language Python for implementation since it is open and there exists a great number of libraries to use. It is well human-readable language and it is fast and easy to write. The calculation speed is not the best but it was sufficient for our purpose. The support for scientific calculations in libraries is also very good. Libraries we have used are: Numpy, Scipy, Sympy, Matplolib and Plotly.

Now we shall explain how the calculation was implemented. We can rewrite the last expression for the EEL spectral function gamma (2.18) in the following form

$$\Gamma_{l_\mathrm{f}}(\omega) = \mathcal{J}(v,\omega) \int \mathrm{d}^2\mathbf{r}_\perp\,\mathrm{d}^2\mathbf{r}'_\perp\,\mathcal{Q}(\mathbf{r},\mathbf{r}')\,\mathcal{K}(\mathbf{r}_\perp,\mathbf{r}'_\perp,\omega,v,\psi_\mathrm{i}), \tag{2.21}$$

where

$$\mathcal{J} = \frac{\hbar e^2}{2\pi^2 v\omega^2 m^2} \tag{2.22}$$

is the prefactor, or "Jack function";

$$\mathcal{Q} = \mathrm{e}^{\mathrm{i}\,l_\mathrm{f}(\phi-\phi')} \int_0^{Q_c} q_{\mathrm{f},r}\,\mathrm{d}q_{\mathrm{f},r}\;J_l(q_{\mathrm{f},r}r)\,J_l(q_{\mathrm{f},r}r') \tag{2.23}$$

called "the Queen function", holds the radial profile of final vortex states and the interaction change of topolological charge; and

$$\mathcal{K} = \left[\nabla_\perp\left\{\psi^*_{\mathrm{i},\perp}(\mathbf{r}_\perp)\right\}; -\mathrm{i}\,q_{z,\mathrm{i}}\psi^*_{\mathrm{i},\perp}(\mathbf{r}_\perp)\right]\cdot\check{\mathcal{G}}(\mathbf{r}_\perp,\mathbf{r}'_\perp,\omega)\cdot[\nabla_\perp\{\psi_{\mathrm{i},\perp}(\mathbf{r}'_\perp)\}; \mathrm{i}\,q_{z,\mathrm{i}}\psi_{\mathrm{i},\perp}(\mathbf{r}'_\perp)] \tag{2.24}$$

called "the King function" holds the inital wafefunctions of vortex and can be thought of as the main interaction part of the EELSF. For great part of the calculation the King and the Queeen were treated separately and the Jack (as it is only a prefactor) was introduced in the end.

Both King and Queen were held in the memory of the computer as numpy arrays of numbers. The calculation (numerical integration of calculated integrand 4D field) had to be performed for each point in the frequency ω domain. Fortunately, the queen is not ω–dependent so in order to save computational time we have preevaluated the Queen for the calculation of whole spectrum with set parameters (such are topological charge, electron energy or speed) and only the King was recalculated for each ω–point.[1]

To set up the computation parameters such are the number of points in space needed or its span we have rendered several plots of Psis, Kings and Queens before running the scripts. Plots are shown in the Fig. [XXX]. We have also ran a convergence test for the number of space points. To get a reasonable compromise between calculation accuracy and computation speed we setteled on 20 nm–30 nm wide field with 50 space points in each of four dimensions (x, y, x', y'). That is 6 250 000 points in total. These computation parameters are well compatible with set parameters of the electron beam with energy 60 keV corresponding to speed $0.446\,c$. We have assumed the beam to have lateral spread of 20 mrad.

Occasionally, when the mesh of our space coincides in some point with the position of specimen, `NaN` (Not a Number) values appear in our fields. Singularities are at these points and the values around them tend to diverge to $\pm\infty$ and python handles them as `NaN`s. This is a problem in numerical integration so we had to use function `numpy.nansum()` which ignores `NaN`s and assumes 0 instead of them.

We have already mentioned that if a particle is polarizable in the crossed way – electrically (magnetically) by magnetic (electric) field, it must always be polarizable in the "pure" way – electrically by electric and magnetically by magnetic field. Thanks to the linearity of expression (2.17), individual contributions from different types of polarizabilities can be calculated separately and we can get the final EELSF as a simple sum of contributions. Dichroism then arises from the crossed electric-magnetic terms. To study dichroism, it is thus convenient to calculate and study the dichroic contribution separately, as we will show later in the Sec. [XXX]

2.3 Results

In the last section of this chapter we present our results in form of spectra. Individiual spectras are commented in their captions. Some interesting results are then discussed more thoroughly in the text.

In the following figures we mostly hold following conventions. 1) The color of line encodes the information about the initial topological charge l_i and its change to the final topological charge l_f. 2) The "density" (dashes, or dots) of the line is lower as the specimen is further away from the center of the vortex.

As we have explained above

[1] The optimization of the computation time was probably the biggest trouble in the implementation process. In the beginning the calculation for approximately 20 ω–points took several days. A smarter way of libraries usage (including not using some of previously used) was needed and we have managed to get the computation time as low as 4 h–8 h per spectrum.

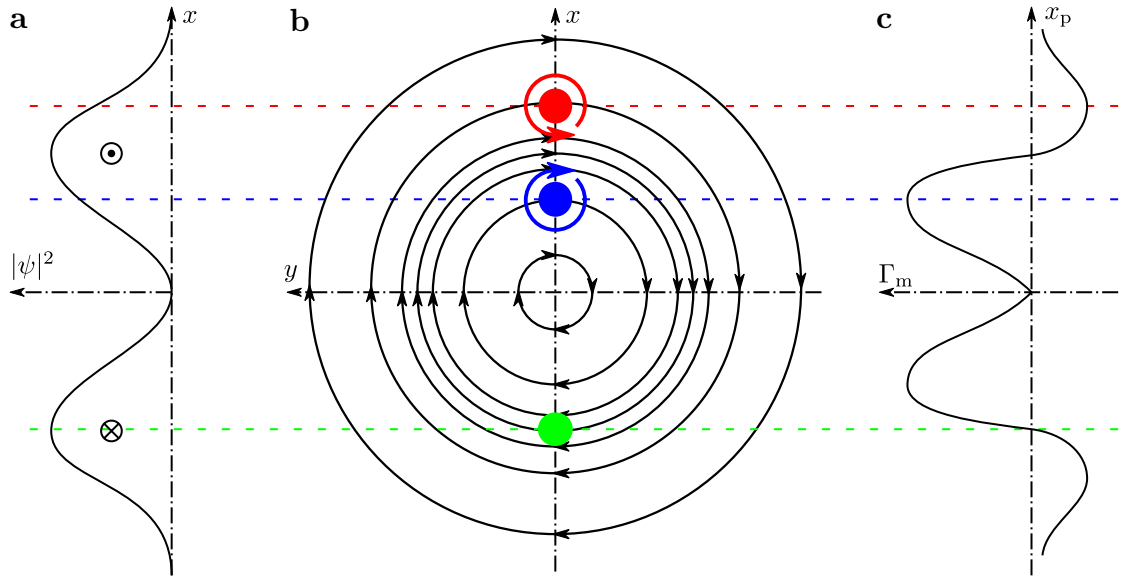

Figure 2.2: Intuition for dependence of response intesity on position of the specimen. a) Probability density of vortex, b) Scheme of vortex circulating around its center. Specimens (in color "feel" the vorticity of the vortex differently depending on their position relative to the main maximum of probability density and can be "spun" in both clockwise and anticlockwise direction. c) Relative magnitude of dichroic response spectrum dependent on the position of specimen.

Chapter 3

Numerical Models

Summary

Appendix A

Notes on Maths

A.1 Paraxial approximation

A.2 Arbitrary constant notation

$$\mathbb{C} + \mathbb{C} = \mathbb{C}, \tag{A.1}$$
$$\mathbb{C} \cdot \mathbb{C} = \mathbb{C}, \tag{A.2}$$
$$a + \mathbb{C} = \mathbb{C}, \tag{A.3}$$
$$a \cdot \mathbb{C} = \mathbb{C} \tag{A.4}$$
$$\tag{A.5}$$

A.3 Square Root Approximation

Assume an expresiion in a form of

$$\sqrt{1+x}, \tag{A.6}$$

where $x \ll 1$. By expanding it with Maclaurin series (Taylor series with the center in 0) we can write

$$\sqrt{1+x} = 1 + \frac{1}{2}x + O(x^2). \tag{A.7}$$

If x is sufficiently small, we can neglect $O(x^2)$ and write

$$\sqrt{1+x} \approxeq 1 + \frac{1}{2}x. \tag{A.8}$$

This approximation rule is widely used in paraxial approximations.

A.4 Cylindrical coordinates

It might be convenient to describe a problem in cylindrical coordinates rather than in Cartesian when there exists some kind of axial symmetry. Let z be the direction of the axis of symmetry. Then any vector $\mathbf{r}$ described by Cartesian coordinates x, y and z can be described by new set of coordinates: radius r and angle of deviation from x axis denoted ϕ together with formerly used z (see Fig. A.1).

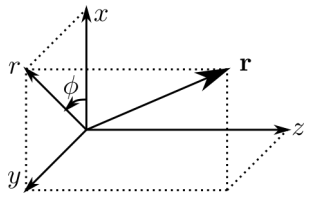

Figure A.1: Cylindrical coordinates.

The transformation equations are

$$\begin{aligned} x &= r\cos\phi, \\ y &= r\sin\phi, \qquad \text{and} \\ z &= z. \end{aligned} \tag{A.9}$$

The inverse transformation rules are

$$\begin{aligned} r &= \sqrt{x^2+y^2}, \\ \phi &= \arctan2(y,x), \qquad \text{and} \\ z &= z. \end{aligned} \tag{A.10}$$

A.5 Evaluation of integral (1.16) using Jacobi–Anger expansion

We will now focus on an integral of form

$$I = \int_0^{2\pi} \mathrm{d}\phi\, \mathrm{e}^{\mathrm{i}\,l\,\phi}\mathrm{e}^{\mathrm{i}\,Q\cos(\phi-\theta)}. \tag{A.11}$$

From [22] we get Jacobi-Anger expansion:

$$\mathrm{e}^{\mathrm{i}\,Q\cos(\phi)} = \sum_{n=-\infty}^{\infty} \mathrm{i}^n\, J_n(Q)\mathrm{e}^{\mathrm{i}\,n\phi} \tag{A.12}$$

Substituting Eq. (A.12) into the Eq. (A.11) and rearranging we get

$$I = \sum_{n=-\infty}^{\infty} \mathrm{i}^n\, \mathrm{e}^{-\,\mathrm{i}\,n\,\theta} J_n(Q) \int_0^{2\pi} \mathrm{d}\phi\, \mathrm{e}^{\mathrm{i}\,l\,\phi}\mathrm{e}^{\mathrm{i}\,n\phi}. \tag{A.13}$$

From residue theorem we can find (for $t \in \langle 0, 2\pi\rangle$), that

$$\int_0^{2\pi} \mathrm{d}\phi\, \mathrm{e}^{\mathrm{i}\,l\,\phi}\mathrm{e}^{\mathrm{i}\,n\phi} = \oint_{z=\mathrm{e}^{\mathrm{i}\,t}} \mathrm{d}z^{n+l-1}(-\,\mathrm{i}) = \delta_{l,-n}. \tag{A.14}$$

This leads to the final result below. In the lasts step we have used [7, Eq. 10.4.1].

$$I = 2\pi\,\mathrm{i}^{-l}\, J_{-l}(Q)\,\mathrm{e}^{\mathrm{i}\,l\,\theta} = 2\pi\,\mathrm{i}^{l}\, J_{l}(Q)\,\mathrm{e}^{\mathrm{i}\,l\,\theta}. \tag{A.15}$$

List of Figures

List of Tables

List of Symbols

List of Abbreviations

1D, 2D, 3D, 4D,... one-, two- three- four-dimensional

CL CathodoLuminiscence,

EELS Electron Energy Loss Spectroscopy,

EELSF Electron Energy Loss Spectral Function,

EM Electromagnetic

OAM Orbital Angular Momentum,

PPP Programmable Phase Plate

SEM Scanning Electron Microscope

STEM Scanning Transmission Electron Microscopy

TEM Transmission Electron Microscopy

VE Vortex Electron, Electron Vortex, can be interchanged with VEB

VEB Vortex Electron Beam

References

[1] F. J. García De Abajo. "Optical excitations in electron microscopy." In: *Reviews of Modern Physics* 82 (1 Feb. 2010), pp. 209–275. ISSN: 00346861. DOI: 10.1103/RevModPhys.82.209.

[2] G. Anzolin et al. "Method to measure off-axis displacements based on the analysis of the intensity distribution of a vortex beam." In: *Physical Review A - Atomic, Molecular, and Optical Physics* 79 (3 Mar. 2009). Preparation of vortex electron beam from plane wave. ISSN: 10502947. DOI: 10.1103/PhysRevA.79.033845.

[3] A. Asenjo-Garcia and F. J. García De Abajo. "Dichroism in the interaction between vortex electron beams, plasmons, and molecules." In: *Physical Review Letters* 113 (6 Aug. 2014). ISSN: 10797114. DOI: 10.1103/PhysRevLett.113.066102.

[4] Richard A. Beth. "Direct Detection of the Angular Momentum of Light." In: *Phys. Rev.* 48 (5 Sept. 1935), pp. 471–471. DOI: 10.1103/PhysRev.48.471. URL: https://link.aps.org/doi/10.1103/PhysRev.48.471.

[5] K. Y. Bliokh et al. *Theory and applications of free-electron vortex states*. May 2017. DOI: 10.1016/j.physrep.2017.05.006.

[6] Michel Bosman et al. "Mapping surface plasmons at the nanometre scale with an electron beam." In: *Nanotechnology* 18.16 (Mar. 2007), p. 165505. DOI: 10.1088/0957-4484/18/16/165505. URL: https://doi.org/10.1088/0957-4484/18/16/165505.

[7] *NIST Digital Library of Mathematical Functions*. F. W. J. Olver, A. B. Olde Daalhuis, D. W. Lozier, B. I. Schneider, R. F. Boisvert, C. W. Clark, B. R. Miller, B. V. Saunders, H. S. Cohl, and M. A. McClain, eds. URL: http://dlmf.nist.gov/.

[8] F. J. García de Abajo and M. Kociak. "Probing the Photonic Local Density of States with Electron Energy Loss Spectroscopy." In: *Phys. Rev. Lett.* 100 (10 Mar. 2008), p. 106804. DOI: 10.1103/PhysRevLett.100.106804. URL: https://link.aps.org/doi/10.1103/PhysRevLett.100.106804.

[9] Jiří Komrska. *Difrakce*. 2007. URL: http://physics.fme.vutbr.cz/~komrska/Difrakce/.

[10] Andrea Konečná et al. *Probing the electromagnetic response of dielectric antennas by vortex electron beams*. 2021. arXiv: 2111.08810 [physics.optics].

[11] Yuuki Noguchi et al. "Efficient Measurement of the Orbital-Angular-Momentum Spectrum of an Electron Beam via a Dammann Vortex Grating." In: *Physical Review Applied* 12 (6 Dec. 2019), p. 064062. ISSN: 23317019. DOI: 10.1103/PhysRevApplied.12.064062.

[12] Lukas Novotny and Bert Hecht. *Principles of Nano-Optics*. 2nd ed. Cambridge University Press, 2012. ISBN: 978-1-107-00546-4.

[13] Albert Polman, Mathieu Kociak, and F. Javier García de Abajo. "Electron-beam spectroscopy for nanophotonics." In: *Nature Materials* 18 (11 Nov. 2019), pp. 1158–1171. ISSN: 14764660. DOI: 10.1038/s41563-019-0409-1.

[14] Koh Saitoh et al. "Production of electron vortex beams carrying large orbital angular momentum using spiral zone plates." In: *Journal of Electron Microscopy* 61.3 (Mar. 2012), pp. 171–177. ISSN: 0022-0744. DOI: 10.1093/jmicro/dfs036. eprint: https://academic.oup.com/jmicro/article-pdf/61/3/171/5854114/dfs036.pdf. URL: https://doi.org/10.1093/jmicro/dfs036.

[15] A. H. Tavabi et al. *Generation of electron vortex beams with over 1000 orbital angular momentum quanta using a tuneable electrostatic spiral phase plate*. 2022. DOI: 10.48550/ARXIV.2203.00477. URL: https://arxiv.org/abs/2203.00477.

[16] Masaya Uchida and Akira Tonomura. "Generation of electron beams carrying orbital angular momentum." In: *Nature* 464 (7289 Apr. 2010), pp. 737–739. ISSN: 00280836. DOI: 10.1038/nature08904.

[17] G. M. Vanacore et al. "Ultrafast generation and control of an electron vortex beam via chiral plasmonic near fields." In: *Nature Materials* 18 (6 June 2019), pp. 573–579. ISSN: 14764660. DOI: 10.1038/s41563-019-0336-1.

[18] J. Verbeeck, H. Tian, and A. Béché. "A new way of producing electron vortex probes for STEM." In: *Ultramicroscopy* 113 (Feb. 2012), pp. 83–87. ISSN: 03043991. DOI: 10.1016/j.ultramic.2011.10.008.

[19] J. Verbeeck, H. Tian, and P. Schattschneider. "Production and application of electron vortex beams." In: *Nature* 467 (7313 Sept. 2010), pp. 301–304. ISSN: 00280836. DOI: 10.1038/nature09366.

[20] Jo Verbeeck, He Tian, and Gustaaf Van Tendeloo. "How to Manipulate Nanoparticles with an Electron Beam?" In: *Advanced Materials* 25 (8 Feb. 2013), pp. 1114–1117. ISSN: 09359648. DOI: 10.1002/adma.201204206. URL: https://onlinelibrary.wiley.com/doi/10.1002/adma.201204206.

[21] Jo Verbeeck et al. "Demonstration of a 2×2 programmable phase plate for electrons." In: *Ultramicroscopy* 190 (2018), pp. 58–65. ISSN: 0304-3991. DOI: https://doi.org/10.1016/j.ultramic.2018.03.017. URL: https://www.sciencedirect.com/science/article/pii/S0304399117305041.

[22] Eric W. Weisstein. *Jacobi-Anger Expansion. From MathWorld–A Wolfram Web Resource*. Last accesed 6 December 2021. 2021. URL: https://mathworld.wolfram.com/Jacobi-AngerExpansion.html.